



Unsaturated edge-anchored Ni single atoms on porous microwave exfoliated graphene oxide for electrochemical CO₂

Yi Cheng^{a,b,1}, Shiyong Zhao^{b,1}, Haobo Li^{c,1}, Shuai He^b, Jean-Pierre Veder^d, Bernt Johannessen^e, Jianping Xiao^c, Shanfu Lu^f, Jian Pan^b, Matthew F. Chisholm^g, Shi-Ze Yang^{g,*}, Chang Liu^{h,*}, Jingguang G. Chenⁱ, San Ping Jiang^{b,*}

^a Department of Environmental Engineering, School of Metallurgy and Environment, Central South University, Changsha, 410083, China

^b Fuels and Energy Technology Institute & Western Australia School of Mines: Minerals, Energy and Chemical Engineering, Curtin University, Perth, WA 6102, Australia

^c Institute of Natural Science, Westlake Institute for Advanced Study, Westlake University, Hangzhou 310024, Peoples Republic of China

^d John de Laeter Centre, Curtin University, Perth, WA 6102, Australia

^e Australian Synchrotron, Clayton, VIC 3168, Australia

^f Beijing Key Laboratory of Bio-inspired Energy Materials and Devices, School of Space and Environment, Beihang University, Beijing, China

^g Materials Science and Technology Division, Oak Ridge National Laboratory, Oak Ridge, TN 37831, United States

^h Shenyang National Laboratory for Materials Science, Institute of Metal Research, Chinese Academy of Sciences, Shenyang, Liaoning 110016, China

ⁱ Department of Chemical Engineering, Columbia University, New York, NY 10027, USA

ARTICLE INFO

Keywords:

Ni single-atom catalysts

Edge-anchored

Defects

Electrochemical CO₂ reduction

Density functional simulation

ABSTRACT

Supported single atom catalysts (SACs), emerging as a new class of catalytic materials, have been attracting increasing interests. Here we developed a Ni SAC on microwave exfoliated graphene oxide (Ni-N-MEGO) to achieve single atom loading of ~6.9 wt%, significantly higher than previously reported SACs. The atomically dispersed Ni atoms, stabilized by coordination with nitrogen, were found to be predominantly anchored along the edges of nanopores (< 6 nm) using a combination of X-ray absorption spectroscopy (XAS) and aberration-corrected scanning transmission electron microscopy (AC-STEM). The Ni-N-MEGO exhibits an onset overpotential of 0.18 V, and a current density of 53.6 mA mg⁻¹ at overpotential of 0.59 V for CO₂ reduction reaction (CO₂RR), representing one of the best non-precious metal SACs reported so far in the literature. Density functional theory (DFT) calculations suggest that the electrochemical CO₂-to-CO conversion occurs more readily on the edge-anchored unsaturated nitrogen coordinated Ni single atoms that lead to enhanced activity toward CO₂RR.

1. Introduction

Electrochemical reduction of CO₂ (CO₂RR) to C1 or C2 chemicals (e.g., CO, HCOOH, CH₄, CH₃OH, C₂H₄, etc) coupled with renewable energy is the most attractive technology in both CO₂ utilization and renewable energy storage [1]. However, directly reducing CO₂ to liquid fuels is hampered by the limited number of electrocatalysts available to selectively produce hydro-carbons, as well as difficulties in the separation and purification of liquid fuels. An alternative strategy is to reduce CO₂ to CO because CO production is kinetically favorable compared with other C1 and C2 products, and CO is a key feedstock for the production of liquid fuels via the well-established Fischer-Tropsch process [2]. Precious metal catalysts such as Au [3,4], Ag [5,6], and Pd

[7,8] have been extensively investigated for electrochemical CO production from CO₂ due to their high activities and low overpotentials, unfortunately their applications are constrained by high cost. Non-precious metal catalysts such as Zn, [9,10] Bi [11] and Sn [12] and their alloys [13] also show activities for electrochemical CO₂-to-CO conversion, while they suffer from high overpotential (η) and slow kinetics.

Single-atom catalysts (SACs) are an emerging class of electrocatalysts that possess electronic structures different from their bulk counterparts. They have demonstrated outstanding activities and selectivities for catalytic reactions such as CO oxidation, [14,15] oxygen reduction [16,17], hydrogen evolution [18,19] and organic synthesis [20–22]. Density functional theory (DFT) calculations showed that single transition metal atoms would be highly selective for the CO₂RR

* Corresponding authors.

E-mail addresses: shize@bnl.gov (S.-Z. Yang), cliu@imr.ac.cn (C. Liu), S.Jiang@curtin.edu.au (S.P. Jiang).

¹ Yi Cheng is the leading author who design the experiment, do the characterization and write up the manuscript, Shiyong Zhao help synthesis the material, and Haobo Li contribute to the DFT calculation. Yi Cheng, Shiyong Zhao, Haobo Li are first co-authors.

<https://doi.org/10.1016/j.apcatb.2018.10.046>

Received 24 June 2018; Received in revised form 12 October 2018; Accepted 20 October 2018

Available online 22 October 2018

0926-3373/© 2018 Elsevier B.V. All rights reserved.

due to its favorable adsorption of carboxyl (*COOH) or formate (*OCHO) over hydrogen (*H) [23,24]. Most recently, Jiang et al. reported that single Ni atomic sites in graphene vacancies can dramatically lower the CO₂ activation barrier, weakening the binding with CO for facile product release [25]. Zhao et al. reported that metal-organic framework (MOF)-derived Ni SAC exhibits a current density of 10.5 mA cm⁻² at an overpotential of 0.89 V for CO₂RR with a Faradaic efficiency of 71.9% [26].

The challenge in the development of efficient SAC-based electrocatalyst is the very low atomic loading (normally less than 2 wt%) due to the limited number of anchoring sites based on conventional physical or chemical synthesis methods [27,28]. The defects created not only provide the anchoring sites for isolated atoms, but also benefit the catalytic activity [29–31]. Dispersion of single-metal atoms on carbon materials with high surface area provides a high volume of anchoring sites, as well as a highly conductive matrix that facilitates the electrochemical catalytic processes [32–35]. Typically, these SACs are prepared through top-down methods that involve annealing metal precursors with carbon materials or precursors to form a metal-carbon composite followed by a subsequent dealloying [17,33,34]. The process generates not only atomically dispersed single atoms, but also a significant amount of metal nanoparticles (NPs) [33,36]. Thus, the fraction of active atomically dispersed metal atoms is still very low because of the inherent tendency of aggregation of metal atoms during the high temperature annealing process [17,33,34]. Li et al. used topo-chemical transformation by carbon layer coating to preserve the Ni-N₄ structures and to avoid agglomeration of Ni atoms, but the Ni single atom loading obtained is only 1.41 wt% [37]. Recently, our group developed a new one-pot pyrolysis soft-template method to synthesize SACs based on atomically-dispersed transition-metals on nitrogen-doped carbon nanotubes (MSA-N-CNTs, where M = Ni, Co, NiCo, CoFe, NiPt) with outstanding metal loading, e.g., 20 wt% in the case of NiSA-N-CNTs [38]. The high Ni single atom loading is attributed to the high concentration of N dopants, which create defects to anchor the atomically dispersed Ni atoms. Nevertheless, due to the formation of multi-walled carbon nanotubes, significant amounts of metal single atoms are trapped in the inner tubes and only a fraction of single atoms anchored at the outmost walls would be active for CO₂RR, which could limit the overall activity [38].

Herein, we employed a highly porous and high surface defect-rich microwave exfoliated graphene oxide, MEGO, as supports to atomically dispersed Ni single atoms with high activity and efficiency for CO₂RR. The results indicate that MEGO provides large surface area and abundant defects on the pore edge as anchoring sites for single atoms, achieving Ni single atom loading as high as 6.9% for electrochemical CO₂RR. The Ni SACs exhibit a mass activity of 53.6 mA mg⁻¹ and a high selectivity of 92.1% at an overpotential (η) of 0.59 V for CO₂RR. DFT calculations suggested that the experimental growth conditions cause the formation of edge-anchored coordinative unsaturated Ni-N active structures, which exhibit higher catalytic activity for CO₂RR compared with the in-plane Ni-N species.

2. Experimental methods

2.1. Preparation of Ni-N-MEGO

Porous three dimensional microwave exfoliated graphene oxide (3D-MEGO) structure was synthesized following a previously reported procedure (supporting information) [39]. The Ni-N-MEGO were prepared by mixing 3 mL 0.1 mol L⁻¹ nickel nitrate ethanol solution with 100 mg MEGO powder through grinding before being dried at 80 °C. The resulting black powder was ground with 2 g urea to obtain a homogenous grey powder. The as-prepared mixture was put into a tube furnace under an NH₃ (100 sccm) atmosphere at 800 °C for 30 min, yielding a black powder. Then the black powder was further treated with 2 M HNO₃ to eliminate nickel nanoparticles, yielding Ni-N-MEGO.

2.2. Catalyst characterization

The morphology of Ni-N-MEGO was studied by transmission electron microscopy (TEM) and high angle annular dark field (HAADF) scanning TEM (STEM) with elemental mapping on a Titan G2 60–300 at 80 kV. The synthesized materials were dispersed using ethanol solution onto TEM grids. The annular dark field images (ADF) were collected using a Nion UltraSTEM100 microscope operated at 60 kV at a beam current of 60 pA. The recorded images were filtered using a Gaussian function (full width half maximum = 0.12 nm) to remove high frequency noise. The convergence half angle of the electron beam was set to be 30 mrad and the inner collection half angle of the ADF images was 51 mrad. The samples were baked at 160 °C overnight before STEM observation. Diffraction data was collected with a Bruker D8 Advance diffractometer operated at 40 kV and 40 mA with Cu K α (2 θ = 1.5406 Å) in the range of 20–90° [40].

X-ray absorption spectroscopy (XAS) measurements were performed at the wiggler XAS Beamline (12ID) at the Australian Synchrotron in Melbourne, Australia using a set of liquid nitrogen cooled Si(111) monochromator crystals. With the beamline optics employed (Si-coated collimating mirror and Rh-coated focussing mirror) the harmonic content of the incident X-ray beam was negligible. XAS measurements were performed at the Ni K-edge (8.3 keV) at < 10 K to minimize thermal disorder and to ensure that the samples were not radiation-damaged. This was confirmed via repetitive quick scanning of the absorption edge for up to 2 h (12 scans, note that a single complete XAS scan took ~1 h). For these measurements, samples were prepared as pellets via mechanical grinding in a cellulose binder using a mortar/pestle. Both fluorescence and transmission spectra were recorded depending on the concentration of Ni in each sample (the validity of this approach was confirmed by comparing the fluorescence and transmission spectrum for one of the samples for which both methods yielded comparable signal-to-noise data).

2.3. Electrochemical performance

The electrocatalytic activity of Ni-N-MEGO catalysts was evaluated for electrochemical CO₂RR in N₂ and CO₂ saturated 0.5 M KHCO₃ solution using linear scan voltammetry (LSV). Electrolyte was first bubbled with N₂ for 5 min and then bubbled with CO₂ for 15 min before experiments. The catalysts loading for LSV was 0.2 mg cm⁻². The electrodes for CO₂ electrolysis were prepared by casting the catalysts-ethanol-Nafion solution (6 mg mL catalysts, 1% Nafion) on carbon paper (1 cm⁻²) with a gas diffusion layer and a catalyst loading of 0.5 mg cm⁻². Ir black on carbon paper (1 cm⁻²) with a loading of 1 mg cm⁻² was used as the counter electrode (The aim of using Ir black as the counter electrode is because Pt will be oxidized, dissolved and precipitated on the working electrode under the electrolysis condition, which may affect the property and performance of the working electrode). The CO₂ electrolysis was conducted in a gas tight electrochemical cell at different potentials for 2 h. The outlet gas was collected with a gas bag for double channel gas chromatography (Shimadzu, GC-2014 Series) analysis.

2.4. Computational details

DFT calculations were performed using Vienna *ab initio* simulation packages (VASP) [41] with the projector-augmented wave (PAW) pseudopotentials [42]. All calculations were based on the same generalized gradient approximation method with the Perdew-Burke-Ernzerhof (PBE) [43] functional for the exchange-correlation term. The plane wave cutoff was set to 400 eV. The convergence of energy and forces were set to 1 × 10⁻⁴ eV and 0.05 eV Å⁻¹, respectively.

The model of graphene sheet edge was simulated with a periodically repeated graphene nanoribbon in rectangular supercells, with the carbon atoms on the edge saturated with hydrogen atoms. The vacuum

thickness in the direction perpendicular and parallel to the ribbon plane was ~ 12 and ~ 20 Å, respectively. The Brillouin zone was sampled by a $2 \times 1 \times 1$ k -point grid with the Monkhorst-Pack [44] scheme. The model of graphene plane was simulated with a periodically repeated graphene layer with a vacuum slab height of 17 Å using a $2 \times 2 \times 1$ Monkhorst-Pack^{iv} k -point sampling. The model of NiPc was based on a cubic cell of 18 Å with gamma point calculations.

The formation energy for Ni-N was calculated as: $E_{\text{tot}} - n_{\text{C}}\mu_{\text{C}} - n_{\text{N}}\mu_{\text{N}} - n_{\text{H}}\mu_{\text{H}} - n_{\text{Ni}}\mu_{\text{Ni}}$, where E_{tot} is the total energy of the graphene nanoribbon embedded with Ni-N structures, n_{C} , n_{N} , n_{H} and n_{Ni} represent the total number of C, N, H, Ni atoms, and μ_{C} , μ_{N} , μ_{H} and μ_{Ni} represent their chemical potentials, respectively. μ_{C} is reference to pristine graphene nanoribbon, μ_{H} is reference to H_2 : $\mu_{\text{H}} = 1/2 \mu(\text{H}_2)$, μ_{Ni} is reference to a Ni atom. The vertical dashed line for μ_{N} in reference to NH_3 was calculated by: $\mu_{\text{N}} = \mu(\text{NH}_3) - 1/2 \mu(\text{N}_2) - 3/2 \mu(\text{H}_2)$.

The adsorption energy of *CO is calculated as: $E_{\text{tot}} - E_{\text{surface}} - \mu_{\text{CO}}$, where E_{tot} is the total energy of the surface with adsorption species, E_{surface} is the energy of bare surface, μ_{CO} is the chemical potential of CO molecule. The free energy of each species is calculated by: $G = E_{\text{DFT}} + \text{ZPE} + \int \text{CvdT} - T\Delta S$, where E_{DFT} is the DFT-optimized total energy, ZPE is the zero-point vibrational energy, $\int \text{CvdT}$ is the heat capacity, T is the temperature (298 K) and ΔS is the entropy change. The simplified solvent stabilization has been applied as: 0.25 eV for *COOH and 0.1 eV for *CO . The reaction energy is defined as the free energy difference between different reaction steps.

3. Results and discussions

3.1. Synthesis and characterization of Ni SAC

The highly porous MEGO support was prepared using microwave treated graphene oxide with a subsequent pore creation (Fig. 1A, supporting information) [39]. The as prepared MEGO possesses a very high surface area of $2649 \text{ m}^2 \text{ g}^{-1}$ and a pore volume of $1.79 \text{ cm}^3 \text{ g}^{-1}$ with an average pore size of 2.7 nm (Fig. S1). Raman spectrum shows a high $I_{\text{D}}/I_{\text{G}}$ (2.57) ratio, revealing the large number of defects formed during the pore creation process (Fig. S1D) [45]. The Ni single atom catalyst was prepared by mixing 3 mL 0.1 mol L^{-1} nickel nitrate in ethanol solution with 100 mg MEGO powder ($\sim 18 \text{ wt\%}$ Ni in MEGO) through vacuum filtration to allow Ni^{2+} infiltrating into the pores. The material was then processed by mixing and grinding with urea before being heated in a tube furnace under an NH_3 atmosphere at 800°C . The resultant powder was thoroughly treated with acid to remove the Ni NPs, forming Ni-N-MEGO.

Ni-N-MEGO exhibits a surface area of $2380 \text{ m}^2 \text{ g}^{-1}$ and a pore volume of 1.68 m^3 with a mean size of 2.6 nm, which is slightly lower than that of MEGO (Fig. S1C). Transmission electron microscope (TEM) images reveal that Ni-N-MEGO exhibits a typical 3D structure connected with bamboo like carbon nanotubes (CNTs) with an outer diameter of $\sim 30 \text{ nm}$ (Fig. 1B). The formation of CNTs may be due to catalytic effect of Ni NPs formed on the MEGO surface, which is confirmed by the TEM image of the catalysts before acid treatment (Fig. S2). Scanning TEM with energy-dispersive X-ray spectroscopy (STEM-EDS) of Ni-N-MEGO shows homogeneously dispersed Ni and N species (Fig. 1C). Ni NPs are not observed, revealing that the Ni NPs have been removed by acid treatment.

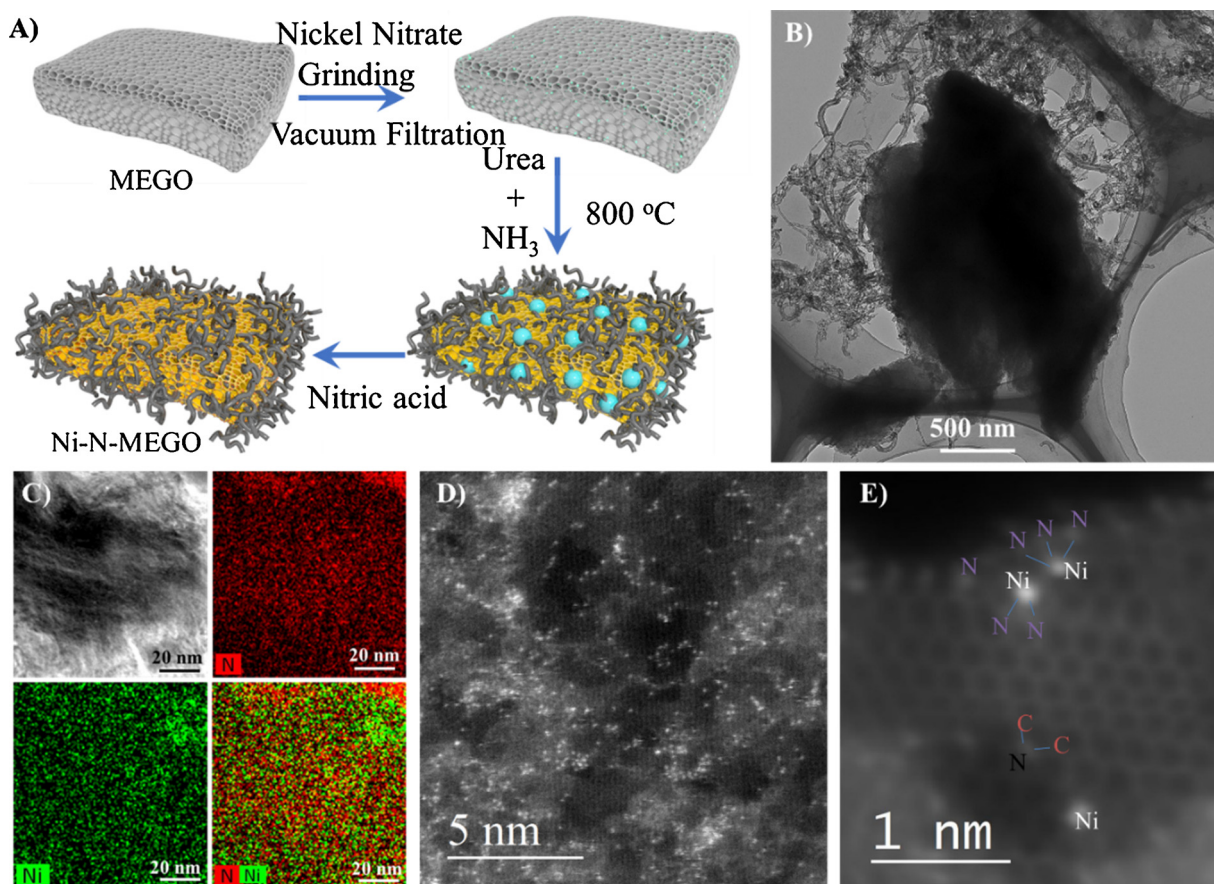


Fig. 1. A) Scheme showing the synthesis of Ni-N-MEGO; B) TEM images of Ni-N-MEGO; C) STEM-EDS mapping of the Ni-N-MEGO; D) AC-STEM image of Ni-N-MEGO showing the porous structure; E) local defects of N dopants and Ni-N_x single atom sites were identified by the atomic column intensity.

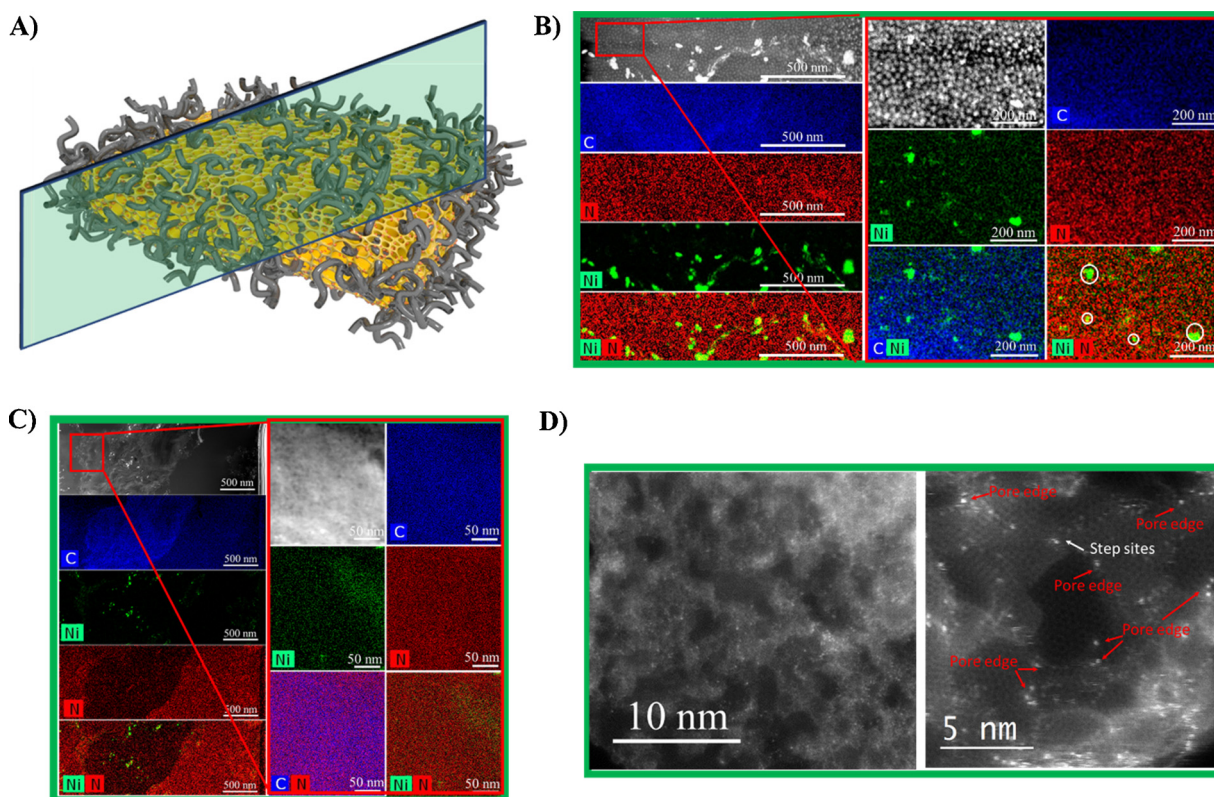


Fig. 2. A) A scheme showing the cross-sections of Ni-N-MEGO structure obtained using a focused ion beam scanning electron microscope (FIB-SEM). STEM-EDS mapping of the cross section of B) Ni-N-MEGO before acid treatment and C) Ni-N-MEGO, D) AC-STEM images showing the single atom Ni sites are predominately anchored on the edges of nanopores inside Ni-N-MEGO.

The atomic dispersion of Ni single atoms was confirmed by aberration-corrected scanning TEM (AC-STEM). The bright dots (Ni atoms) are evenly distributed across the MEGO structure (Fig. 1D and Fig. S3). The imperfect stacking of graphene layers creates high volume micropores with sizes less than 6 nm, consistent with the cryo-nitrogen adsorption measurements. AC-STEM images show imperfect stacking structure with clear Morrie patterns, i.e., the surface atomic layers have a different crystal structure than that in the bulk (Fig. S3A). Those imperfectly stacked graphene layers should produce more grain boundary edges with anchor sites for single atoms. The AC-STEM images clearly show Ni single atoms are predominately anchored on the edge of the pores, exposed basal-plane edges and the steps of graphene sheets (Fig. 1E and Fig. S3B). Two elements with intensities higher than carbon were observed, which could be assigned to Ni and N by considering the synthesis environment and the following XAS results. Most N dopants adjacent to the Ni single atoms were found near the edges of pores, revealing that the unsaturated Ni at the edge coordinated with N species.

Cross-sections of the Ni-N-MEGO structure were obtained using a focused ion beam and scanning electron microscope (FIB-SEM, Fig. 2). Before acid treatment, Ni NPs with sizes in the range of 15–80 nm were formed on the surface and in the bulk of MEGO structure (Fig. S2 and Fig. 2B). Apart from the large Ni NPs, the cross section of MEGO shows a highly patterned flake-like structure. The flakes with sizes less than 15 nm are typically rich in Ni and N in contrast to the bright NPs, which are simply rich in Ni (Fig. 2B, white circle). The formation of large Ni NPs is related to the high concentration of Ni^{2+} precursor absorbed in large pores (> 50 nm) in the MEGO, which result in preferential formation of Ni NPs. Ni^{2+} is encapsulated in the small sized nanopores (less than 6 nm) that lead to a preferential formation of Ni-N single atom on the edge of pores. The cross section of Ni-N-MEGO further confirms that all surface NPs and the majority of the larger NPs inside

the MEGO are removed by an acid treatment (Fig. 2C), as indicated by the disappearance of the flake structures and large NPs. The C, N and Ni elements are uniformly distributed across the structure, revealing the atomically dispersed Ni species both inside and on the surface. The AC-STEM images clearly show that the Ni single sites are predominately anchored on the edge of the pores, exposed basal-plane edges and steps of graphene sheets inside the MEGO (Fig. 2D).

The chemical environments of Ni-N-MEGO were examined by X-ray absorption spectroscopy (X-ray absorption near edge structure, XANES, and X-ray absorption fine structure, XAFS, Fig. 3). The Ni L-edge shows typically two groups of peaks around 850–860 eV ($\text{L}_{3\text{-edge}}$) and 868–876 eV ($\text{L}_{2\text{-edge}}$) due to the splitting of the Ni 2p orbitals (Fig. 3A). The Ni $\text{L}_{3\text{-edge}}$ of the Ni-N-MEGO shows a major peak at 854.4 eV and a small shoulder at 852.9 eV. The intense peak at ~ 854.4 eV for Ni-N-MEGO is very close to that of nickel phthalocyanine (NiPc, ~ 854.2 eV), but very different from Ni in Ni foil (Ni^0 , 852.8 eV), NiO (852.9 eV) or $\text{Ni}(\text{OH})_2$ (853.1 eV). This evidently indicates that the Ni in N-MEGO is mainly coordinated with N rather than Ni-Ni, Ni-O or Ni-OH. The Ni-N-MEGO exhibits a broad peak (Fig. 3A and Fig. S4A), indicating that the Ni single atoms exhibit a more complex coordination environment compared to NiPc which is purely Ni-N_4 . The N K-edge of Ni-N-MEGO (Fig. 3B) shows two peaks at 398.6 eV and 401.5 eV, assigned to pyridinic and graphitic N, respectively, consistent with that of N-MEGO. [46] Different from that of N-MEGO, the new feature of Ni-N-MEGO centered at 399.4 eV can be assigned to Ni-N-C species, [38] and the new peak at 403.7 eV is likely attributed to N-O [47]. Compared to a Ni foil (Ni^0), the rising-edge of Ni K-edge XANES spectra shift to higher energies and indicate an increase in the oxidation state of Ni in the case of Ni-N-MEGO (Fig. S4B). The Fourier-transformed extended X-ray absorption fine structure reveals that NiPc shows a sharp peak centering at 1.43 Å (Fig. 3C), consistent with the well-defined Ni-N_4 species. [48] However, in the case of Ni-N-MEGO, a broader peak around 1.42 Å is observed, which is consistent with Ni-N coordination [26]. However,

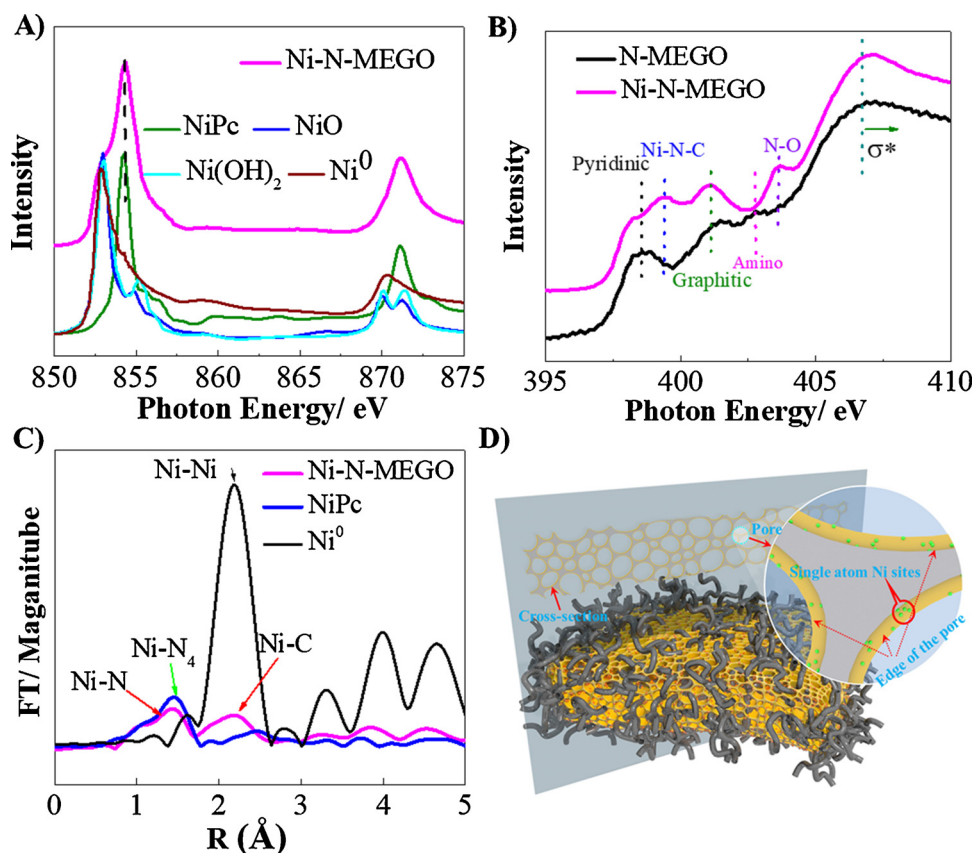


Fig. 3. Chemical environment of Ni-N-MEGO as probed via X-ray absorption spectroscopy. A) Ni L-edge spectra of Ni-N-MEGO compared with NiPc, Ni(OH)₂, NiO and Ni foil (Ni⁰); B) N K-edge spectra of EXAFS spectra of Ni-N-MEGO compared with N-MEGO; C) Fourier transform of the EXAFS spectra of Ni-N-MEGO and nickel foil (Ni⁰); and D) The scheme shows the distribution of the Ni single atoms on the edges of the pores in Ni-N-MEGO.

the intensity of the peak at 1.42 Å is lower than that of NiPc, likely due to the formation of unsaturated Ni-N₂, Ni-N₃ and well-defined Ni-N₄ species. Further, the broad peaks at 2.30 Å is likely contributed by the presence trace amount of Ni NPs (Ni-Ni at 2.15 Å).

The content of the atomically dispersed Ni atoms was estimated by the combination of inductively coupled plasma (ICP) and linear combination analysis (LCA) of the Ni L-edge. The ICP results reveal that the Ni species in the Ni-N-MEGO are estimated to be ~8.3 wt%. LCA of the Ni L-edge reveals that Ni-N-MEGO is mainly composed of Ni-N (83.8%) species with a small contribution of Ni⁰ (8.6%) and Ni(OH)₂ (7.7%) (Fig. S5, Table S1). Thus, the total Ni single atoms in the Ni-N-MEGO is estimated to be ~6.9 wt%, significantly higher than the metal-organic framework (MOF) derived SACs (1.53 wt%) [26], Ni(I)-NSG (4.6 wt%) [49] (Table S2).

3.2. Electrochemical CO₂ reduction

The electrochemical activity of Ni-N-MEGO for CO₂RR was investigated in N₂- and CO₂-saturated 0.5 M KHCO₃ solution (Fig. 4A). A significantly higher current density was obtained in CO₂-saturated solution as compared to that in N₂-saturated solution for Ni-N-MEGO with an onset potential of -0.29 V vs RHE (reversible hydrogen electrode), i.e., $\eta = 0.18$ V. Ni-N-MEGO exhibits a better activity for CO₂RR with suppressed H₂ evolution as compared to NiPc supported on graphene, NiPc-G, and N-MEGO (Fig. 4B-D). The CO yield increases with the increase of cathodic potentials (Fig. 4C). On Ni-N-MEGO catalysts, the CO yield is as high as 4.66×10^{-3} mmol cm⁻² min⁻¹ at potential of -0.55 V ($\eta = 0.44$ V) with suppressed H₂ yield (5.6×10^{-4} mmol cm⁻² min⁻¹). The CO yield of Ni-N-MEGO is 4 and 2 times higher than that of N-MEGO and NiPc-G, respectively. The corresponding current density, j_{CO} , for CO₂RR on Ni-N-MEGO is 4.6, 16.3 and 26.8 mA cm⁻² (9.2, 32.6 and 53.6 mA mg⁻¹) at $\eta = 0.29$, 0.44 and 0.59 V, respectively (Fig. 4D). This is significantly higher than non-precious metal catalysts such as Zn (4 mA cm⁻² at $\eta = 0.69$ V) [10]

measured under similar test conditions, and also comparable or even better than noble metal catalysts such as Au [3,50,51], and Ag [5,6] (Table S3). For example, Zhu et al. reported that gold NPs achieves a j_{CO} value of 3.1 mA mg⁻¹ at $\eta = 0.44$ V [4]. Our Ni-N-MEGO outperforms the single Ni atom counterparts due to its high loading of Ni single atoms (Table 1). For example, the MOF-derived Ni SACs with a Ni single atom loading of 1.53 wt% show a current density of 2.94 mA mg⁻¹ (7.35 mA cm⁻²) at $\eta = 0.89$ V [26], the Ni and N doped nanofiber produced by electrospinning with a Ni single atom loading of 1.6 wt% shows a j_{CO} of 20 mA mg⁻¹ at $\eta = 0.7$ V [25], and Ni single atoms coordinated with four N on carbon with a single atom loading of 1.41 wt% exhibits a current density of 28.6 mA cm⁻² at $\eta = 0.771$ V [37]. The turnover frequency (TOF) of Ni-N-MEGO was calculated to be 0.04, 0.14 and 0.24 s⁻¹ at $\eta = 0.29$, 0.44 and 0.59 V (Fig. S6), respectively. The TOF of Ni-N-MEGO is comparable to the best noble metal based catalysts for electrochemical CO₂-to-CO conversion such as nanoporous Ag (0.002 s⁻¹ @ $\eta = 0.39$ V), ultrathin Au NWs (0.02 s⁻¹ @ $\eta = 0.24$ V) and other protoporphyrin-based homogeneous catalysts (< 0.1 s⁻¹) [52,53] and similar to that of 0.22 s⁻¹ at $\eta = 0.59$ V of MOF derived Ni SAC [26] (Table S3). The Faraday efficiency (FE, Fig. 4E) of Ni-N-MEGO is 72.5%, 78.4%, 89.0% and 92.1% at -0.3, -0.4, -0.55 and -0.7 V, respectively, significantly higher than those of NiPc-G and N-MEGO with a FE only around 40–71%, further revealing the outstanding performance of Ni-N-MEGO. The preliminary stability of Ni-N-MEGO for CO₂RR was tested at -0.55 V (Fig. 4F). The initial current density was ~19.3 mA cm⁻², and decreased by 29.1% to ~13.7 mA cm⁻² after polarization for 21 h. Nevertheless, the FE of electrochemical CO₂-to-CO conversion remains at ~89%, showing that the Ni-N-MEGO is reasonably stable for the electrochemical reduction CO₂ to CO.

In the Ni-N-MEGO, there are four types of species could be the active sites for electrochemical CO₂ reduction, Ni single atoms coordinated with nitrogen (Ni-N), nitrogen doped carbon (N-C, eg, pyridinic and graphitic N), Ni nanoparticles, Ni single atoms coordinated with carbon

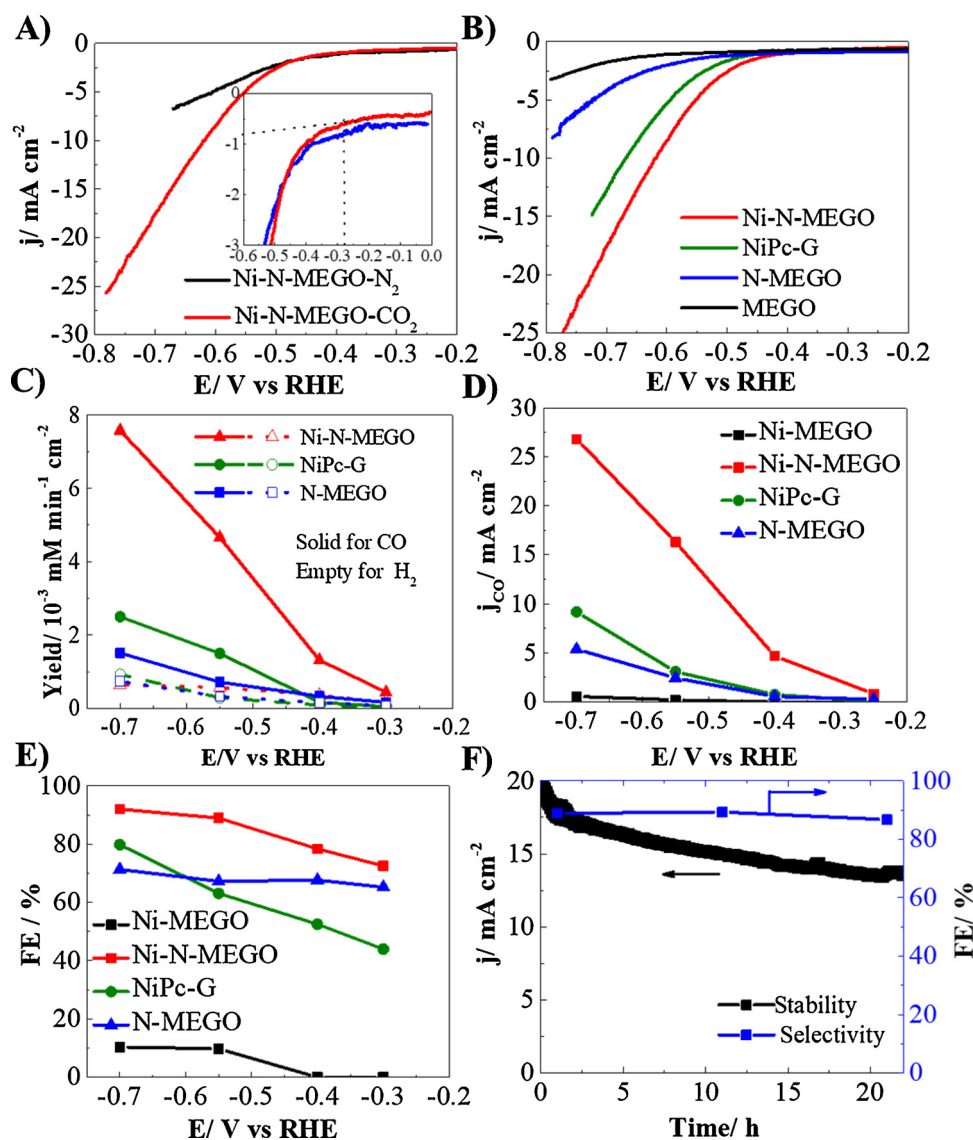


Fig. 4. CO₂ reduction performance. Linear scan voltammetry (LSV) curves of A) Ni-N-MEGO in N₂ and CO₂ saturated 0.5 M KHCO₃ solution, and B) Ni-N-MEGO, NiPc, N-MEGO and MEGO in CO₂ saturated 0.5 M KHCO₃ solution. Plots of C) product yields and D) j_{CO} and E) Faradaic efficiency of CO at -0.30 , -0.40 , -0.55 and -0.7 V on Ni-N-MEGO, NiPc, N-MEGO and/or Ni-MEGO electrodes. F) Preliminary stability of Ni-N-MEGO electrodes. The CO₂RR was conducted in CO₂ saturated 0.5 M KHCO₃ solution with catalysts loading of 0.5 mg cm^{-2} . The potential is IR corrected.

(Ni-C). N-C exhibits activity for CO₂ to CO conversion, but the current density is very low (Fig. 4B-D), which is consistent with the reported results [54,55]. A comparison of the Ni-N-MEGO and Ni-N-MEGO

before acid treatment has been revealed with similar j_{CO} , but the FE for Ni-N-MEGO before acid treatment is only 60–83%, which is lower than that of 72–92% for Ni-N-MEGO (Fig. S7). The results indicate the Ni

Table 1

Summarized CO₂RR electrochemical activity of NiSA reported so far with the results in this work.

Materials	Test condition		CO ₂ RR		References
	Electrolyte	Loading	E _{onset} (V vs RHE)	j _{CO}	
Ni-N-MEGO	0.5 M KHCO ₃	6.7 wt%	−0.29	26.8 mA cm ^{−2} @ −0.70 V	This work
Ni-N-Gr	0.1 M KHCO ₃	2.2 wt%	−0.50	3 mA cm ^{−2} @ −0.80 V	[62]
NiSAs/N-C	0.5 M KHCO ₃	1.53%	−0.57	10.48 mA cm ^{−2} @ −1.00 V	[26]
NiN-GS	0.1 M KHCO ₃	–	−0.35	4 mA cm ^{−2} @ −0.80 V	[25]
Ni-NG	0.5 M KHCO ₃	0.44 at%	−0.31	11 mA cm ^{−2} @ −0.73 V	[63]
Ni-N ₄ -C	0.5 M KHCO ₃	1.41 wt%	−0.40	36.2 mA cm ^{−2} @ −0.91 V	[37]
C-Zn _x Ni _y ZIF-8	1 M KHCO ₃	5.44 wt%	−0.40	71.5 mA cm ^{−2} @ −1.03 V	[64]
A-Ni-NG	0.5 M KHCO ₃	4.0 wt%	−0.20		[49]
A-Ni-NSG	0.5 M KHCO ₃	2.5 wt%	−0.15	22.5 mA cm ^{−2} @ −0.72 V	
NiSA-N-CNT	0.5 M KHCO ₃	20.7 wt%	−0.27	4.0 mA cm ^{−1-2} @ −0.4 V	[61]

nanoparticles are not contributed to CO₂RR but hydrogen evolution, consistent with the reported results [56,57]. In order to investigate the activity of Ni-C, a Ni-MEGO has been prepared with a similar procedure of preparation of Ni-N-MEGO without nitrogen source, and the Ni single atoms with mass loading less than 2% coordinated with the defects of the carbon matrix has been obtained on the edge of the pores (Fig. S8A–C), while the electrochemical study shows that the Ni-C species are not active for electrochemical CO₂ reduction but with preferential activity for hydrogen evolution reaction (Fig. 4D and E and Fig. S8D). These results all confirm that the Ni-N species are the major active species that contributed to CO₂ electrochemical reduction.

3.3. Density functional theory simulation

DFT calculations were performed in order to understand the structure of Ni-N active sites. A model of graphene nanoribbon with the edge substituted with N atoms and embedded with Ni atoms has been built to simulate the single Ni atoms anchored on graphene edge, while a graphene plane embedded with Ni-N structures was used to simulate the in-plane Ni-N sites for comparison. Considering that various adsorption structures on the single Ni atoms is possible under the reaction environment of catalyst synthesis, several different structures with Ni-N coordination number of 2–4 have been considered and their formation energies were calculated to evaluate the stability (Fig. 5A, we define Ni coordinated with 4 nitrogen is saturated Ni-N₄, and the coordination number less than 4 is unsaturated Ni-N species). As shown in Fig. 5B, under N-rich (e.g. N₂) conditions (right side) the edge-anchored 4-coordinate structures (NiN₄, NiN₂(NH₂)₂) are more stable, while the Ni-N

structures with lower coordination numbers (NiN₂, NiN₂(NH₂)) become more stable as the chemical potential of N (μ_N) decreases under H-rich conditions (left side). In our case, the materials were synthesized in NH₃ reducing atmosphere (vertical dashed line), the edge-anchored Ni-N₄ edge species and the coordinatively edge-anchored unsaturated Ni-N species such as NiN₂, NiN₂(NH₂), NiN₂(NH₂)₂ and NiN₃ should be preferentially generated in NH₃ conditions. These calculations are consistent with our AC-STEM image, Ni L-edge and Ni K-edge results, which indicate that the unsaturated Ni-N are generated at the edge of the pores of MEGO structure.

The mechanism for CO₂RR to CO has been considered with three steps: an adsorption step (CO₂ → *COOH), a conversion step on the surface (*COOH → *CO) and a desorption step (*CO → CO). The binding free energy of CO (G_{*CO}) is a good descriptor for the reactivity on metal sites [34]. As shown in Fig. 5C, the reaction energy shows a linear correlation with G_{*CO} , exhibiting straight lines for both the adsorption and desorption steps. According to the Sabatier principle [35], the optimal activity is achieved at an intermediate adsorption strength, that is, the intersection points of the steps (shown in yellow). Among the different Ni-N active sites studied, 4-coordinate structures (NiN₄ plane and NiN₄ edge) are unfavorable for the adsorption step (red) and 2-coordinate structures (NiN₂) is unfavorable for the desorption step (blue), 3-coordinate edge-anchored structures (NiN₃ and NiN₂(NH₂)) exhibit highest reactivity due to the favorable energy for both the adsorption of CO₂ and the desorption of CO (Fig. S9), while the in-plane NiN₃ is unfavorable for desorption of CO. Note that NiN₂(NH₂) and NiN₃ are also quite stable under experimental conditions (Fig. 5B), suggesting that they are the major active sites in the Ni-N-MEGO for

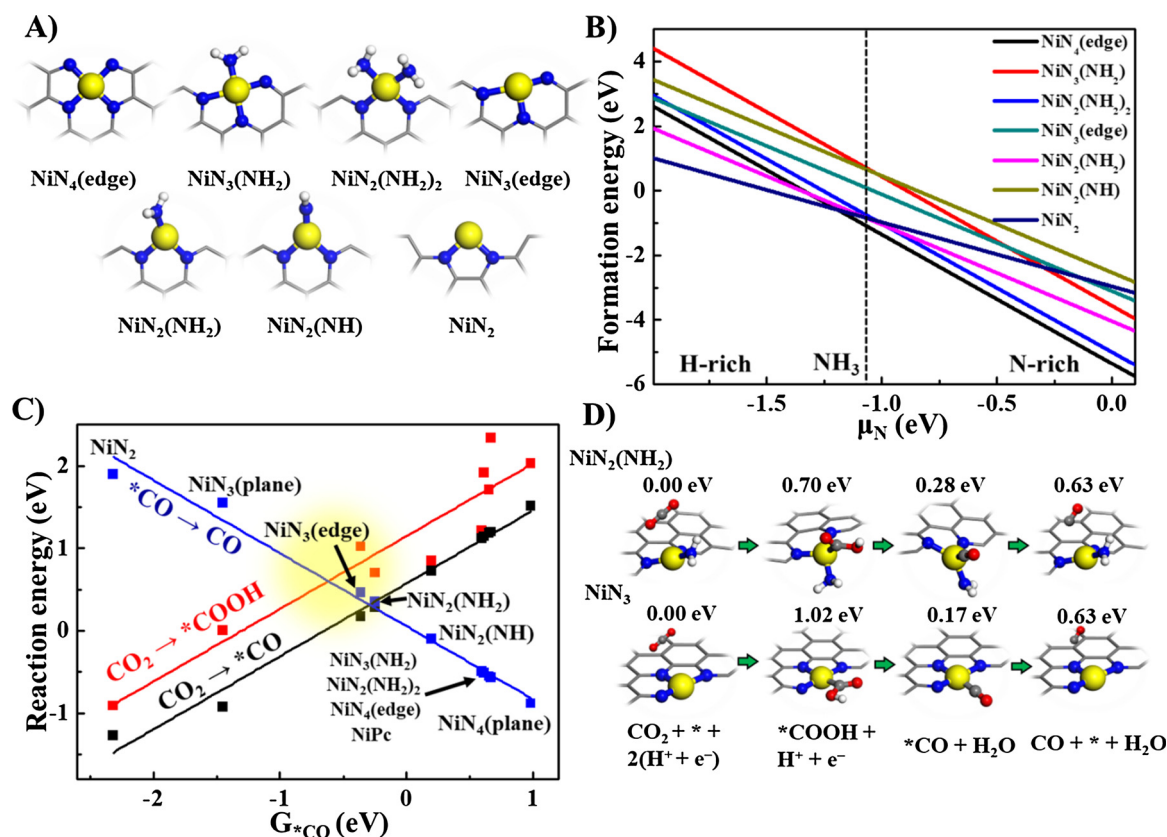


Fig. 5. DFT calculation results. A) different Ni-N active site structures on the edges of graphene sheets, B) formation energies as function of chemical potential for nitrogen (μ_N) for different Ni-N active site structures. A lower formation energy indicates better stability. The vertical dashed line locates where the N source is referenced to NH₃. C) The reaction energy is in linear relationship with the adsorption free energy of *CO (G_{*CO}) on the active sites. A lower reaction energy indicates higher reactivity. Different Ni-N structures were located in the lines. A lower G_{*CO} indicates weaker adsorption. The region around the intersection point of the higher adsorption and desorption steps (shown in yellow) indicates the optimal reactivity. D) Reaction pathway on the NiN₂(NH₂) and NiN₃ site, with the free energy shown on top. (C: grey; N: blue; Ni: yellow; O: red; H: white). (For interpretation of the references to colour in this figure legend, the reader is referred to the web version of this article.)

electrochemical CO₂RR. The reaction pathway with free energy on edge-anchored unsaturated NiN₃ and NiN₂(NH₂) was then shown in Fig. 5D, which show the intermediate energy of 0.7 and 1.02 eV for CO₂ activation (CO₂ → *COOH), and 0.63 and 0.63 eV for CO desorption (*CO → CO), respectively.

Single atom catalysts are strongly constrained by the loading mainly due to the low surface area and limited number of defects that can stabilize the single atoms. Our method creates a high surface area (2649 m² g^{−1}) MEGO structure with high volume of pores with an average size of 2.7 nm. The defect-rich small sized pores provide multi-function roles: a) Since only limited amount of Ni precursors are absorbed in the small sized pores through vacuum filtration, the precursors could efficiently contact with the nitrogen sources such as NH₃ and urea during the high temperature annealing process resulting in a preferential formation of the Ni-N species [33], which is evidenced by the high density of Ni and N elements in the small pores and the formation of Ni particles in the large pores (Fig. 2B). b) The small size pores provide a confinement effect that prevents the aggregation of Ni atoms during the high temperature annealing process [26,58]. c) The pores expose graphene edges with abundant defects that could anchor single Ni atoms. Due to these reasons the single atom Ni is distributed in the entire MEGO structure with loading estimated to be ~6.9 wt%. The loading is significantly higher than the metal-organic framework (MOF) derived SACs (1.53 wt%) [26], Ni(I)-NSG (4.6 wt%) [49], and also higher than the atomically dispersed Fe-N (2.9 wt%) supported on carbon materials prepared by template-induced methods [33]. The loading achieved in the current work is among the highest single atom loading reported to date in the area of non-precious metal-based SACs (Table S2). Our DFT calculations reveal that the edge-sites of NiN₄, NiN₂(NH₂), NiN₂(NH₂)₂ and NiN₂ are energetically favourable to form under the NH₃ atmosphere (formation energy lower than 0 eV), then followed by NiN₃ (Fig. 5B). These results are consistent with previous observations that edge-anchored Fe-N structures show lower formation energies and increased stability than in-plane FeN₄ structures [59,60]. Thus, the high loading of single Ni atoms in the high surface area MEGO results from a large number of edges and defects around the pores that could stabilize Ni single atoms.

Ni single atoms anchored with nitrogen have attracted enormous attention recently [37,49,25,61]. Normally, the in-plane NiN₄ is considered as the active center for CO₂RR [37,49,61]. However, Zhao et al. proposed that the in-plane NiN₃ could be responsible for CO₂RR [26]. Our DFT results reveal that the in-plane NiN₄ exhibits significantly higher energy for CO₂ activation (2.03 eV, CO₂ → *COOH) compared with edge NiN₄, while in-plane NiN₃ is quite unfavorable for CO desorption (1.52 eV, *CO → CO) (Fig. 5 and Fig. S9), disclosing that these in-plane Ni-N structures should be less active for CO₂RR compared with edge-anchored structures. The edge-anchored saturated NiN₄ is better than the corresponding in-plane NiN₄, but still exhibits high energy for CO₂ activation (1.71 eV, CO₂ → *COOH). In contrast, the edge-anchored unsaturated NiN₂ center turns out not favorable for CO desorption due to the high binding energy (1.82 eV) of the CO on NiN₂, even though it shows favorable energy for CO₂ → *COOH and *COOH → *CO. The edge-anchored NiN₃, NiN₂(NH₂) structures with moderate degree of unsaturation exhibits optimized energies for CO₂ activation and CO desorption, as the intermediates binding to these edge-anchored unsaturated moieties are neither too strong nor too weak. Bear in mind that NiN₄, NiN₂(NH₂), NiN₂(NH₂)₂, NiN₂ and NiN₃ are preferentially formed under the NH₃ atmosphere, we could propose that the edge-anchored unsaturated NiN₂(NH₂) and NiN₃ sites could be the best active sites for CO₂ reduction to CO, followed by the edged NiN₂(NH₂)₂ and NiN₄, while NiN₂ should be less active due to the strong binding energy of CO.

4. Conclusions

Here we successfully tailored the edge structures of porous carbon

with Ni single atoms. The porous structure with a high surface area (2649 m² g^{−1}) provided large number of anchor sites for single Ni atoms and the nanopores (< 6 nm) also help prevent aggregation and stabilize the single atom Ni-N species during high temperature annealing. The unsaturated edge anchored Ni single sites with loading as high as 6.9% show a mass activity of 53.6 mA mg^{−1} and a high selectivity of 92.1% at an overpotential of 0.59 V for CO₂RR. The DFT results identify that the edge-anchored unsaturated three nitrogen coordinated Ni single atoms exhibit better activity for CO₂RR compared with in-plane structures, and the high CO₂RR activity originates from the high loading of unsaturated Ni single atoms on edges. Our results provide a new avenue to develop highly efficient noble-metal-free SACs with high loading for electrocatalysis.

Acknowledgements

This research was supported by the Australian Research Council Discovery Project Funding Scheme (project number: DP150102044, DP180100731 and DP180100568). The authors acknowledge the facilities, and the scientific and technical assistance of the National Imaging Facility at the Centre for Microscopy, Characterization & Analysis, the University of Western Australia, and the WA X-Ray Surface Analysis Facility, funded by an Australian Research Council LIEF grant (LE120100026). The technical support and scientific advice provided by B. Cowie and L. Thompsen regarding XANES measurements are acknowledged. XAS measurements were performed on the soft X-ray and XAS beamlines of the Australian Synchrotron, Victoria, Australia, part of ANSTO. The electron microscopy carried out at ORNL (S.Z.Y. and M.F.C) was supported by the U.S. Department of Energy, Office of Science, Basic Energy Sciences, Materials Science and Engineering and through a user proposal supported by ORNL's Center for Nanophase Materials Sciences, which is sponsored by the Scientific User Facilities Division of U.S. Department of Energy. CL thanks the support from National Natural Science Foundation of China (Nos. 51521091). We would like to show our gratitude to Dr Jian Pan who has helped with the schematic graphs. Yi Cheng designed the experiment, do the characterization and write up the manuscript, Shiyong Zhao helped synthesis the material, and Haobo Li contribute to the DFT calculation. Author 1, Author 2 and Author 3 contributed equally to this work.

Appendix A. Supplementary data

Supplementary data associated with this article can be found, in the online version, at <https://doi.org/10.1016/j.apcatb.2018.10.046>.

References

- [1] B. Kumar, J.P. Brian, V. Atla, S. Kumari, K.A. Bertram, R.T. White, J.M. Spurgeon, New trends in the development of heterogeneous catalysts for electrochemical CO₂ reduction, *Catal. Today* 270 (2016) 19–30.
- [2] D.J. Wilhelm, D.R. Simbeck, A.D. Karp, R.L. Dickenson, Syngas production for gas-to-liquids applications: technologies, issues and outlook, *Fuel Process. Technol.* 71 (2001) 139–148.
- [3] H. Mistry, R. Reske, Z. Zeng, Z.-J. Zhao, J. Greeley, P. Strasser, B.R. Cuenya, Exceptional size-dependent activity enhancement in the electroreduction of CO₂ over Au nanoparticles, *J. Amer. Chem. Soc.* 136 (2014) 16473–16476.
- [4] W. Zhu, R. Michalsky, Ö. Metin, H. Lv, S. Guo, C.J. Wright, X. Sun, A.A. Peterson, S. Sun, Monodisperse Au nanoparticles for selective electrocatalytic reduction of CO₂ to CO, *J. Amer. Chem. Soc.* 135 (2013) 16833–16836.
- [5] M. Ma, B.J. Trzeźniewski, J. Xie, W.A. Smith, Selective and efficient reduction of carbon dioxide to carbon monoxide on oxide-derived nanostructured silver electrocatalysts, *Angew. Chem. Int. Ed.* 55 (2016) 9748–9752.
- [6] Q. Lu, J. Rosen, Y. Zhou, G.S. Hutchings, Y.C. Kimmel, J.G. Chen, F. Jiao, A selective and efficient electrocatalyst for carbon dioxide reduction, *Nat. Commun.* 5 (2014) 3242.
- [7] D. Gao, H. Zhou, J. Wang, S. Miao, F. Yang, G. Wang, J. Wang, X. Bao, Size-Dependent electrocatalytic reduction of CO₂ over Pd nanoparticles, *J. Amer. Chem. Soc.* 137 (2015) 4288–4291.
- [8] W. Sheng, S. Kattel, S. Yao, B. Yan, Z. Liang, C.J. Hawxhurst, Q. Wu, J.G. Chen, Electrochemical reduction of CO₂ to synthesis gas with controlled CO/H₂ ratios,

- Energy Environ. Sci. 10 (2017) 1180–1185.
- [9] D.H. Won, H. Shin, J. Koh, J. Chung, H.S. Lee, H. Kim, S.I. Woo, Highly efficient, selective, and stable CO₂ electroreduction on a hexagonal Zn catalyst, *Angew. Chem. Int. Ed.* 55 (2016) 9297–9300.
 - [10] J. Rosen, G.S. Hutchings, Q. Lu, R.V. Forest, A. Moore, F. Jiao, Electrodeposited Zn dendrites with enhanced CO selectivity for electrocatalytic CO₂ reduction, *ACS Catal.* 5 (2015) 4586–4591.
 - [11] Z. Zhang, M. Chi, G.M. Veith, P. Zhang, D.A. Lutterman, J. Rosenthal, S.H. Overbury, S. Dai, H. Zhu, Rational design of Bi nanoparticles for efficient electrochemical CO₂ reduction: the elucidation of size and surface condition effects, *ACS Catal.* 6 (2016) 6255–6264.
 - [12] J. Medina-Ramos, R.C. Pupillo, T.P. Keane, J.L. DiMeglio, J. Rosenthal, Efficient conversion of CO₂ to CO using tin and other inexpensive and easily prepared post-transition metal catalysts, *J. Amer. Chem. Soc.* 137 (2015) 5021–5027.
 - [13] Z. Yin, D. Gao, S. Yao, B. Zhao, F. Cai, L. Lin, P. Tang, P. Zhai, G. Wang, D. Ma, X. Bao, Highly selective palladium-copper bimetallic electrocatalysts for the electrochemical reduction of CO₂ to CO, *Nano Energy* 27 (2016) 35–43.
 - [14] B. Qiao, A. Wang, X. Yang, L.F. Allard, Z. Jiang, Y. Cui, J. Liu, J. Li, T. Zhang, Single-atom catalysis of CO oxidation using Pt₁/FeO_x, *Nat. Chem.* 3 (2011) 634–641.
 - [15] J. Liu, F.R. Lucci, M. Yang, S. Lee, M.D. Marcinkowski, A.J. Therrien, C.T. Williams, E.C.H. Sykes, M. Flytzani-Stephanopoulos, Tackling CO poisoning with single-atom alloy catalysts, *J. Amer. Chem. Soc.* 138 (2016) 6396–6399.
 - [16] S. Yang, J. Kim, Y.J. Tak, A. Soon, H. Lee, Single-atom catalyst of platinum supported on titanium nitride for selective electrochemical reactions, *Angew. Chem. Int. Ed.* 55 (2016) 2058–2062.
 - [17] P. Chen, T. Zhou, L. Xing, K. Xu, Y. Tong, H. Xie, L. Zhang, W. Yan, W. Chu, C. Wu, Y. Xie, Atomically dispersed Iron–Nitrogen species as electrocatalysts for bifunctional oxygen evolution and reduction reactions, *Angew. Chem. Int. Ed.* 56 (2017) 610–614.
 - [18] H.J. Qiu, Y. Ito, W. Cong, Y. Tan, P. Liu, A. Hirata, T. Fujita, Z. Tang, M. Chen, Nanoporous graphene with single-atom nickel dopants: an efficient and stable catalyst for electrochemical hydrogen production, *Angewandte Chemie* 127 (2015) 14237–14241.
 - [19] N. Cheng, S. Stambula, D. Wang, M.N. Banis, J. Liu, A. Riese, B. Xiao, R. Li, T.-K. Sham, L.-M. Liu, G.A. Botton, X. Sun, Platinum single-atom and cluster catalysis of the hydrogen evolution reaction, *Nat. Commun.* 7 (2016) 13638.
 - [20] B. Zhang, H. Asakura, J. Zhang, J. Zhang, S. De, N. Yan, Stabilizing a platinum single-atom catalyst on supported phosphomolybdic acid without compromising hydrogenation activity, *Angew. Chem. Int. Ed.* 55 (2016) 8319–8323.
 - [21] L. Wang, W. Zhang, S. Wang, Z. Gao, Z. Luo, X. Wang, R. Zeng, A. Li, H. Li, M. Wang, X. Zheng, J. Zhu, W. Zhang, C. Ma, R. Si, J. Zeng, Atomic-level insights in optimizing reaction paths for hydroformylation reaction over Rh/CoO single-atom catalyst, *Nat. Commun.* 7 (2016) 14036.
 - [22] R. Lang, T. Li, D. Matsumura, S. Miao, Y. Ren, Y.-T. Cui, Y. Tan, B. Qiao, L. Li, A. Wang, X. Wang, T. Zhang, Hydroformylation of olefins by a rhodium single-atom catalyst with activity comparable to RhCl(PPh₃)₃, *Angew. Chem. Int. Ed.* 55 (2016) 16054–16058.
 - [23] S. Back, J. Lim, N.Y. Kim, Y.H. Kim, Y. Jung, Single-atom catalysts for CO₂ electroreduction with significant activity and selectivity improvements, *Chem. Sci.* 8 (2017) 1090–1096.
 - [24] H. He, Y. Jagvaral, Electrochemical reduction of CO₂ on graphene supported transition metals – towards single atom catalysts, *Phys. Chem. Chem. Phys.* 19 (2017) 11436–11446.
 - [25] K. Jiang, S. Siahrostami, A.J. Akey, Y.B. Li, Z.Y. Lu, J. Lattimer, Y.F. Hu, C. Stokes, M. Gangishetty, G.X. Chen, Y.W. Zhou, W. Hill, W.B. Cai, D. Bell, K.R. Chan, J.K. Norskov, Y. Cui, H.T. Wang, Transition-metal single atoms in a graphene shell as active centers for highly efficient artificial photosynthesis, *Chem* 3 (2017) 950–960.
 - [26] C. Zhao, X. Dai, T. Yao, W. Chen, X. Wang, J. Wang, J. Yang, S. Wei, Y. Wu, Y. Li, Ionic exchange of metal–organic frameworks to access single nickel sites for efficient electroreduction of CO₂, *J. Amer. Chem. Soc.* 139 (2017) 8078–8081.
 - [27] J. Liu, Catalysis by supported single metal atoms, *ACS Catal.* 7 (2017) 34–59.
 - [28] X.-F. Yang, A. Wang, B. Qiao, J. Li, J. Liu, T. Zhang, Single-atom catalysts: a new frontier in heterogeneous catalysis, *Acc. Chem. Res.* 46 (2013) 1740–1748.
 - [29] Y. Wang, M. Qiao, Y. Li, S. Wang, Tuning surface electronic configuration of NiFe LDHs nanosheets by introducing cation vacancies (Fe or Ni) as highly efficient electrocatalysts for oxygen evolution reaction, *Small* 14 (2018) 1800136.
 - [30] S. Dou, L. Tao, R. Wang, S. El Hankari, R. Chen, S. Wang, Plasma-assisted synthesis and surface modification of electrode materials for renewable energy, *Adv. Mater.* 30 (2018) 1705850.
 - [31] L. Zhang, Y. Jia, G. Gao, X. Yan, N. Chen, J. Chen, M.T. Soo, B. Wood, D. Yang, A. Du, X. Yao, Graphene defects trap atomic Ni species for hydrogen and oxygen evolution reactions, *Chem* 4 (2018) 285–297.
 - [32] Y. Zheng, Y. Jiao, Y. Zhu, Q. Cai, A. Vasileff, L.H. Li, Y. Han, Y. Chen, S.-Z. Qiao, Molecule-Level g-C₃N₄ coordinated transition metals as a new class of electrocatalysts for oxygen electrode reactions, *J. Amer. Chem. Soc.* 139 (2017) 3336–3339.
 - [33] Y.J. Sa, D.-J. Seo, J. Woo, J.T. Lim, J.Y. Cheon, S.Y. Yang, J.M. Lee, D. Kang, T.J. Shin, H.S. Shin, H.Y. Jeong, C.S. Kim, M.G. Kim, T.-Y. Kim, S.H. Joo, A general approach to preferential formation of active Fe–Nx sites in Fe–N/C electrocatalysts for efficient oxygen reduction reaction, *J. Amer. Chem. Soc.* 138 (2016) 15046–15056.
 - [34] D. Deng, X. Chen, L. Yu, X. Wu, Q. Liu, Y. Liu, H. Yang, H. Tian, Y. Hu, P. Du, R. Si, J. Zhou, X. Cui, H. Li, J. Xiao, T. Xu, J. Deng, F. Yang, P.N. Duchesne, P. Zhang, J. Zhou, L. Sun, J. Li, X. Pan, X. Bao, A single iron site confined in a graphene matrix for the catalytic oxidation of benzene at room temperature, *Sci. Adv.* 1 (2015) e1500462.
 - [35] H. Yan, H. Cheng, H. Yi, Y. Lin, T. Yao, C. Wang, J. Li, S. Wei, J. Lu, Single-atom Pd₁/Graphene catalyst achieved by atomic layer deposition: remarkable performance in selective hydrogenation of 1,3-Butadiene, *J. Amer. Chem. Soc.* 137 (2015) 10484–10487.
 - [36] W.-J. Jiang, L. Gu, L. Li, Y. Zhang, X. Zhang, L.-J. Zhang, J.-Q. Wang, J.-S. Hu, Z. Wei, L.-J. Wan, Understanding the high activity of Fe–N–C electrocatalysts in oxygen reduction: Fe/Fe₃C nanoparticles boost the activity of Fe–Nx, *J. Amer. Chem. Soc.* 138 (2016) 3570–3578.
 - [37] W. X. Li, M. Bi, Y. Chen, H. Sun, W. Ju, J. Yan, X. Zhu, W. Wu, C. Chu, Y. Xie Wu, Exclusive Ni–N₄ sites realize near-unity CO selectivity for electrochemical CO₂ reduction, *J. Amer. Chem. Soc.* 139 (2017) 14889–14892.
 - [38] Y. Cheng, S. Zhao, B. Johannessen, J.P. Veder, M. Saunders, M.R. Rowles, M. Cheng, C. Liu, M.F. Chisholm, R. De Marco, H.M. Cheng, S.Z. Yang, S.P. Jiang, Atomically dispersed transition metals on carbon nanotubes with ultrahigh loading for selective electrochemical carbon dioxide reduction, *Adv. Mater.* 30 (2018) e1706287.
 - [39] Y. Zhu, S. Murali, M.D. Stoller, K.J. Ganesh, W. Cai, P.J. Ferreira, A. Pirkle, R.M. Wallace, K.A. Cychosz, M. Thommes, D. Su, E.A. Stach, R.S. Ruoff, Carbon-Based supercapacitors produced by activation of graphene, *Science* 332 (2011) 1537–1541.
 - [40] S. Zhao, Y. Cheng, J.-P. Veder, B. Johannessen, M. Saunders, L. Zhang, C. Liu, M.F. Chisholm, R. De Marco, J. Liu, S.-Z. Yang, S.P. Jiang, One-pot pyrolysis method to fabricate carbon nanotube supported Ni single-atom catalysts with ultrahigh loading, *ACS Applied Energy Materials* (2018).
 - [41] G. Kresse, J. Furthmüller, Efficient iterative schemes for ab initio total-energy calculations using a plane-wave basis set, *Phys. Rev. B* 54 (1996) 11169–11186.
 - [42] P.E. Blöchl, Projector augmented-wave method, *Phys. Rev. B* 50 (1994) 17953–17979.
 - [43] J.P. Perdew, K. Burke, M. Ernzerhof, Generalized gradient approximation made simple, *Phys. Rev. Lett.* 77 (1996) 3865–3868.
 - [44] H.J. Monkhorst, J.D. Pack, Special points for Brillouin-zone integrations, *Phys. Rev. B* 13 (1976) 5188–5192.
 - [45] L.M. Malard, M.A. Pimenta, G. Dresselhaus, M.S. Dresselhaus, Raman spectroscopy in graphene, *Phys. Rep.* 473 (2009) 51–87.
 - [46] H.B. Yang, J. Miao, S.F. Hung, J. Chen, H.B. Tao, X. Wang, L. Zhang, R. Chen, J. Gao, H.M. Chen, L. Dai, B. Liu, Identification of catalytic sites for oxygen reduction and oxygen evolution in N-doped graphene materials: development of highly efficient metal-free bifunctional electrocatalyst, *Sci. Adv.* 2 (2016) e1501122.
 - [47] J. Zhong, J.-J. Deng, B.-H. Mao, T. Xie, X.-H. Sun, Z.-G. Mou, C.-H. Hong, P. Yang, S.-D. Wang, Probing solid state N-doping in graphene by X-ray absorption near-edge structure spectroscopy, *Carbon* 50 (2012) 335–338.
 - [48] L.A. Avakyan, A.S. Manukyan, A.A. Mirzakhanyan, E.G. Sharoyan, Y.V. Zubavichus, A.L. Trigub, N.A. Kolpacheva, L.A. Bugaev, Atomic structure of nickel phthalocyanine probed by X-ray absorption spectroscopy and density functional simulations, *Opt. Spectrosc.* 114 (2013) 347–352.
 - [49] H.B. Yang, S.-F. Hung, S. Liu, K. Yuan, S. Miao, L. Zhang, X. Huang, H.-Y. Wang, W. Cai, R. Chen, J. Gao, X. Yang, W. Chen, Y. Huang, H.M. Chen, C.M. Li, T. Zhang, B. Liu, Atomically dispersed Ni(ii) as the active site for electrochemical CO₂ reduction, *Nat. Energy* 3 (2018) 140–147.
 - [50] Y. Chen, C.W. Li, M.W. Kanan, Aqueous CO₂ reduction at very low overpotential on oxide-derived Au nanoparticles, *J. Amer. Chem. Soc.* 134 (2012) 19969–19972.
 - [51] W. Zhu, Y.-J. Zhang, H. Zhang, H. Lv, Q. Li, R. Michalsky, A.A. Peterson, S. Sun, Active and selective conversion of CO₂ to CO on ultrathin Au nanowires, *J. Amer. Chem. Soc.* 136 (2014) 16132–16135.
 - [52] J.E. Pander, A. Fogg, A.B. Bocarsly, Utilization of electropolymerized films of cobalt porphyrin for the reduction of carbon dioxide in aqueous media, *ChemCatChem* 8 (2016) 3536–3545.
 - [53] C. Costentin, S. Drouet, M. Robert, J.-M. Savéant, A local proton source enhances CO₂ electroreduction to CO by a molecular Fe catalyst, *Science* 338 (2012) 90–94.
 - [54] J. Wu, R.M. Yadav, M. Liu, P.P. Sharma, C.S. Tiwari, L. Ma, X. Zou, X.-D. Zhou, B.I. Yakobson, J. Lou, P.M. Ajayan, Achieving highly efficient, selective, and stable CO₂ reduction on nitrogen-doped carbon nanotubes, *ACS Nano* 9 (2015) 5364–5371.
 - [55] S. Liu, H. Yang, X. Huang, L. Liu, W. Cai, J. Gao, X. Li, T. Zhang, Y. Huang, B. Liu, Identifying active sites of nitrogen-doped carbon materials for the CO₂ reduction reaction, *Adv. Funct. Mater.* 28 (2011) 1800499.
 - [56] D.S. Hall, C. Bock, B.R. MacDougall, The electrochemistry of metallic nickel: oxides, hydroxides, hydrides and alkaline hydrogen evolution, *J. Electrochem. Soc.* 160 (2013) F235–F243.
 - [57] M. Gong, W. Zhou, M.-C. Tsai, J. Zhou, M. Guan, M.-C. Lin, B. Zhang, Y. Hu, D.-Y. Wang, J. Yang, S.J. Pennycook, B.-J. Hwang, H. Dai, Nanoscale nickel oxide/nickel heterostructures for active hydrogen evolution electrocatalysis, *Nat. Commun.* 5 (2014) 4695.
 - [58] S. Wang, Q. Zhao, H. Wei, J.-Q. Wang, M. Cho, H.S. Cho, O. Terasaki, Y. Wan, Aggregation-free gold nanoparticles in ordered mesoporous carbons: toward highly active and stable heterogeneous catalysts, *J. Amer. Chem. Soc.* 135 (2013) 11849–11860.
 - [59] E.F. Holby, G. Wu, P. Zelenay, C.D. Taylor, Structure of Fe–Nx–C defects in oxygen reduction reaction catalysts from first-principles modeling, *The Journal of Physical Chemistry* (2018).
 - [60] E.F. Holby, P. Zelenay, Linking structure to function: the search for active sites in non-platinum group metal oxygen reduction reaction catalysts, *Nano Energy* 29 (2016) 54–64.
 - [61] Y. Cheng, S. Zhao, B. Johannessen, J.P. Veder, M. Saunders, M.R. Rowles, M. Cheng, C. Liu, M.F. Chisholm, R. De Marco, H.M. Cheng, S.Z. Yang, S.P. Jiang, Atomically

- dispersed transition metals on carbon nanotubes with UltraHigh loading for selective electrochemical carbon dioxide reduction, *Adv. Mater.* 30 (13) (2018) 1706287.
- [62] P. Su, K. Iwase, S. Nakanishi, K. Hashimoto, K. Kamiya, Nickel-nitrogen-modified graphene: an efficient electrocatalyst for the reduction of carbon dioxide to carbon monoxide, *Small* 12 (2016) 6083–6089.
- [63] K. Jiang, S. Siahrostami, T. Zheng, Y. Hu, S. Hwang, E. Stavitski, Y. Peng, J. Dynes, M. Gangisetty, D. Su, K. Attenkofer, H. Wang, Isolated Ni single atoms in graphene nanosheets for high-performance CO₂ reduction, *Energy Environ. Sci.* 11 (4) (2018) 893–903.
- [64] H. C. Yan, Y. Li, H. Ye, F. Wu, R. Cai, J. Si, S. Xiao, S. Miao, F. Xie, Y. Yang, G. Li, X. Bao Wang, Coordinatively unsaturated nickel–nitrogen sites towards selective and high-rate CO₂ electroreduction, *Energy Environ. Sci.* 11 (2018) 1204–1210.